Sains Malaysiana 52(10)(2023): 2955-2970
http://doi.org/10.17576/jsm-2023-5210-17

Effects of High-Energy Electron Beam Irradiation on the Structure, Composition and Morphological Properties of Graphene Nanoplatelet Films

(Kesan Penyinaran Rasuk Elektron Bertenaga Tinggi pada Struktur, Komposisi dan Sifat Morfologi Filem *Nanoplatelet* Grafin)

NURUL HIDAYAH MOHAMAD NOR[1,2,*], NUR AFIRA ANUAR[1], NOOR AZRINA TALIK[1], WAN AHMAD TAJUDDIN WAN ABDULLAH[2], KRITSADA KITTIMANAPUN[3], HIDEKI NAKAJIMA[3], NARONG CHANLEK[3], MOHD FAKHARUL ZAMAN RAJA YAHYA[4] & BOON TONG GOH[1]

[1]*Low Dimensional Material Research Centre, Department of Physics, Faculty of Science, Universiti Malaya, 50603 Kuala Lumpur, Malaysia*
[2]*National Centre for Particle Physics, Universiti Malaya, 50603 Kuala Lumpur, Malaysia*
[3]*Synchrotron Light Research Institute, Nakhon Ratchasima 30000, Thailand*
[4]*Faculty of Applied Science, Universiti Teknologi MARA, 40450 Shah Alam, Selangor, Malaysia*

Received: 18 August 2023/Accepted: 21 September 2023

ABSTRACT

This work demonstrated the effects of 1.2 GeV high-energy electron beam irradiation on a few-layers of graphene (FLG) and multi-layer graphene (MLG) films grown via an in-house hot wire chemical vapour deposition (HWCVD) system. The FLG and MLG films were grown on highly doped n-type c-Si (100) substrates which were pre-treated using argon plasma (50 W) for 1 min and 10 min, respectively. The as-prepared samples were then irradiated using a 1.2 GeV high-energy electron beam with a dosage of 1.2×10^9 e^-/cm^2 at atmospheric and room temperature ambient conditions. The effects of the irradiation-mediated defects on the carbon lattice structure of both graphene samples were validated from the decreased sp^2 C=C carbon content, and the increase in the adventitious carbon contamination C-O-C content. Raman results showed an elevation of the I_D/I_G ratio and blue-shift of the 2D and G band peaks for both the irradiated samples, which validated the mediated defects due to the dislocation of carbon atoms in the graphene sheets. The blue-shifted of 2D and G peaks were much more significant in the MLG than FLG which may indicate a better self-reconstructing property for the MLG atomic network, compared to the FLG. The stability of the films against high-energy electron beam irradiation was validated by their conductivity and surface topography. In conclusion, HWCVD grown graphene nanoplatelet films have high potential for graphene-based high-energy charged particle detectors.

Keywords: Graphene; high-energy electron beam; HWCVD; nanoplatelets; radiation tolerance

ABSTRAK

Kajian ini menunjukkan kesan penyinaran radiasi elektron bertenaga tinggi 1.2 GeV pada beberapa lapisan grafin (FLG) dan berbilang lapisan grafin (MLG) yang dihasilkan melalui kaedah wayar panas pemendapan wap kimia (HWCVD). Filem FLG dan MLG dihasilkan pada permukaan substrat c-Si (100) jenis-n berdop tinggi yang telah dirawat terlebih dahulu menggunakan plasma argon (50 W) selama 1 minit dan 10 minit. Sampel yang telah disediakan kemudiannya disinari menggunakan radiasi elektron bertenaga tinggi 1.2 GeV dengan dos 1.2×10^9 e^-/cm^2 pada keadaan atmosfera dan suhu bilik. Kesan radiasi dalam menghasilkan kecacatan pada struktur kekisi karbon kedua-dua sampel grafin telah disahkan daripada pengurangan kandungan karbon sp^2 C=C serta peningkatan kandungan kontaminasi karbon adventif C-O-C. Analisis Raman menunjukkan peningkatan nisbah I_D/I_G dan anjakan-biru bagi puncak jalur 2D dan G untuk kedua-dua sampel yang disinari, yang mengesahkan kecacatan pengantara disebabkan oleh kehelan atom karbon dalam helaian grafin. Anjakan-biru puncak 2D dan G adalah lebih ketara dalam MLG berbanding FLG yang mungkin menunjukkan sifat membina semula diri yang lebih baik untuk rangkaian atom MLG, berbanding FLG. Kestabilan filem terhadap penyinaran radiasi elektron bertenaga tinggi telah disahkan oleh kekonduksian dan topografi permukaannya. Kesimpulannya, filem nanoplatelet grafin yang dihasilkan menggunakan kaedah HWCVD ini mempunyai potensi tinggi untuk menghasilkan pengesan zarah bercas tenaga tinggi berasaskan grafin.

Kata kunci: Grafin; HWCVD; *nanoplatelet*; sinaran elektron bertenaga tinggi; toleransi radiasi

Introduction

Since the discovery of the first two-dimensional material by Andre Geim and Konstantin Novoselov in 2004, graphene has received a great attention because of its excellent properties, and great potential to be applied in nanoelectronics technology, especially in sensors and detectors. It exhibited excellent Young's modulus, intrinsic strength, thermal conductivity, sheet resistance, and electron mobility (Lee et al. 2008). High electron density, outstanding thermal conductivity (Moser, Barreiro & Bachtold 2007) and excellent electron mobility contribute to the excellent potential of graphene as a superb candidate for high-energy and high-tension detectors and sensors. Graphene is known to work with high cut-off frequencies (1 GHz), which proves its ability to produce quick responses during detection (Lin et al. 2009). The study of graphene in gas detectors, chemical detectors, and biomolecular detectors (Ang et al. 2008; Kim et al. 2008; Lu, Ocola & Chen 2009; Robinson et al. 2008; Schedin et al. 2007; Zhang et al. 2010) has previously been reported, however, its application in high-energy detection experiments remains unexplored. The application of graphene in this field offers exciting advantages, such as producing thin and flexible detectors which can be directly integrated with electronics in pixel sizes and provides low maintenance costs compared to the current state-of-art detectors (Serry et al. 2015). A simulation study on the application of MLG as detector material in high-energy physics application was performed as previously reported (Nor et al. 2022).

The interaction between high energy particles and materials not only produce defects such as atomic displacement, but also results in electronic excitations (Shulman & Ginell 1970). Although few studies have discussed the effects of particle/ions irradiation with graphene, most of the research focused on the low energy range only to understand the interaction mechanism (Kang et al. 2022; Warbinek et al. 2019). Recently, few studies have been reported on the effect of high-energy irradiation (Kinetic energy >10 KeV) with graphene. Slobodian et al. (2018) reported that the knock-on collision resulted in carbon atoms displacement for interaction with high-energy charged particles. Childres et al. (2010) demonstrated the impact of 30 keV electron beam irradiation on a single-layer graphene prepared from mechanical exfoliation-based graphite. The study showed that electron irradiation resulted in n-type doping, and created defects in the graphene, which changed its transport properties and reduced the carrier's mobility. At the same time, lower energy (5-20 keV) of electron irradiation was demonstrated to introduce defects to the single-layer and bilayer of graphene samples which were prepared using mechanical exfoliation-based graphite (Teweldebrhan & Balandin 2009). Meanwhile, Liu, Teweldebrhan and Balandin (2011) reported that energetic electron irradiation introduced lattice defects to the graphene network due to altered electrical and structural properties of the single-layer and bilayer graphene. On the other hand, Lee et al. (2016) reported an increase in the conductivity of graphene after irradiation with 5 MeV protons due to the strong hole-doping that increase the hole-density by 10-times and the dc-resistance decreased by 60% from the initial condition. However, it should be noted that most studies focus on energy lower than 10 MeV and single-layer or one thick atomic graphene only. Most graphene mentioned also requires a transfer process from the substrate, forming more defects introduced from the transfer process.

In this work, a few-layers of graphene (FLG) and multi-layer graphene (MLG) films were prepared using an in-house hot wire chemical vapour deposition (HWCVD) system. The effect of high-energy electron irradiation of 1.2 GeV on the different graphene structures (i.e., FLG and MLG) was investigated with an intensity of up to 1.2×10^9 e^-/cm^2. The effects of high-energy electron irradiation on the lattice structure, chemical contents, and electrical properties of the irradiated graphene films are discussed.

Materials and Methods

Preparation of graphene samples

The FLG and MLG samples were directly grown on highly doped n-type crystal silicon (c-Si) substrates with a (100) orientation using an in-house HWCVD system, as previously reported by Anuar et al. (2021). The substrates were prepared (2.5 cm × 2.5 cm) whilst a coiled tungsten (W) wire (99.95% purity and 0.5 mm diameter) was used as the hot-filament and was connected to the voltage reulator (IBC Regavolt 1P-1kVA 0-240 V A.C). The experimental processes were divided into two parts; the argon (Ar) ion plasma, and the graphene deposition processes. The Ar ion plasma process was performed to deposit W nanoparticles on the crystal Silicon (c-Si) substrates. The W nanoparticles acted as an effective metal catalyst particle to facilitate the growth across a large-area, and provide a controllable thickness of graphene layers in either the FLG or MLG. This can

be done by varying the Ar ion plasma duration from 1 to 10 min, which resulted in nanoparticle grains size of 7.4 and 24.3 nm. The parameter settings used for Ar ion plasma were as follows: i) duration: 1-10 min; ii) process pressure: 0.4 mbar; iii) substrate temperature: 450 °C; iv) Ar gas flow rate: 10 sccm; v) radio-frequency power: 50 W and vi) filament temperature: 1600 °C.

After the plasma process, the deposition process was subsequently carried out by switching off the mass flow controller of the Ar gas and radio-frequency power, introducing methane (CH_4) and hydrogen (H_2) gases into the chamber and maintaining the gases at 10 and 200 sccm, respectively. The filament temperature was quickly increased to 2200 °C to sufficiently decompose the CH_4 and H_2, whilst the substrate temperature remained at 450 °C.

HIGH-ENERGY ELECTRON BEAM EXPERIMENTAL SETUP

The as-prepared FLG and MLG samples were exposed to a high-energy electron beam of 1.2 GeV for 10 h using The Beam Test Facility (BTF) in the Synchrotron Light Research Institute (SLRI), Nakhon Ratchasima, Thailand. The properties of the electron beams obtained from the synchrotron booster at the High-energy Beam Transport Line (HBT) are shown in the Table 1 (Kittimanapun et al. 2018, 2016). Figure 1(a) depicts the schematic diagram of the high-energy electron irradiation process at the BTF, while Figure 1(b) shows the actual picture of the BTF setup, and the sample's position during the beam test. The beam size and sample size for this test were 3.1 mm × 1.7 mm and 2.5 cm × 2.5 cm, respectively. The characterisation for both samples were carried out after the irradiation.

CHARACTERIZATION OF FLG AND MLG

The chemical states of the FLG and MLG (the as-prepared and irradiated samples) were examined using X-ray photoemission spectroscopy (XPS) at the photoemission spectroscopy (PES) beamline centre, BL3.2Ua, which was located at SLRI, Thailand. The PES system combined with Thermo VG Scientific CLAM2 electron spectrometer was operated at 600 eV, with an energy step of 0.1 eV. The binding energies were then calibrated using the C 1s energy of 284.6 eV (Greczynski & Hultman 2020). The high-resolution scan at the C 1s band was deconvoluted to possible C-related bands representing the chemical states for the as-prepared and irradiated samples. The fitting of the C 1s band was performed using the Gaussian fitting function in MS Excel, which was provided by the beamline, BL3.2U. The XPS measurements for the irradiated FLG and MLG were subsequently conducted just after the beam test to avoid any further contamination.

The Raman spectra of the as-prepared and irradiated samples were produced using the InVia Raman microscope with a diffraction grating (2400 lines/mm) and a charge-coupled device detector. An Ar ion laser (514 nm and 5 mW) was used to produce an effective laser irradiation spot area of 2 μm in diameter and was carefully calibrated using an internal single-crystal silicon at 520 cm^{-1}. Owing to the ultra-thin thicknesses of the FLG and MLG, the measurement was conducted using 10 % of the laser power (equivalent to 5 mW), for 30 s in the range between 1000 and 100 cm^{-1}. The D, G, and 2D band peak parameters (peak position, Full-width Half Maximum (FWHM), and intensity) were obtained using the Origin Pro curve fitting method.

TABLE 1. The working parameters of the BTF at the SLRI

Particle	Electron
Energy	up to 1.2 GeV
Energy spread	-0.05 %
Current	~10 mA
Repetition rate	every 2 s
No. of electron per bunch	between 10^6 and 10^5
Pulse duration	8.5 ns
Beam size	~ 3.1 mm × 1.7 mm

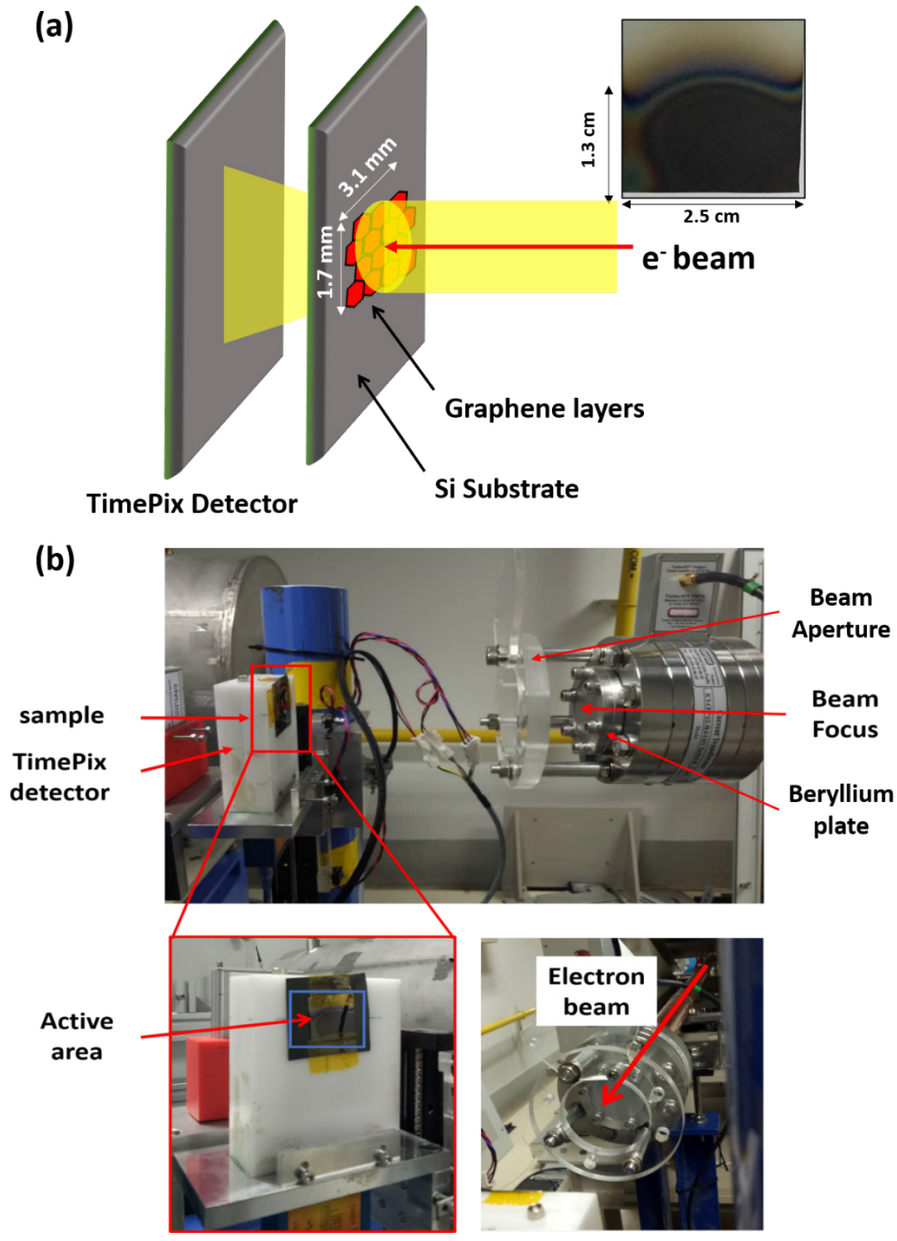

FIGURE 1. (a) Schematic diagram of the high-energy electron beam irradiation on graphene sample. Inset represent a real graphene film (darker area) on Si (111) substrate. (b) Actual photographs of the high-energy electron beam test setup, and the positions of graphene sample and electron beams output and apertures

The current-voltage curves of the as-prepared and irradiated samples were determined using the four-point probe (JANDEL Universal Probe). A tungsten carbide needle with a 0.5 mm diameter was used in this measurement. The sheet resistance was calculated from a voltage drop curve, resulting from the applied current on the outer probes, following the Equation (1) as follows:

$$Rs = \frac{\pi}{\ln(2)} \frac{\Delta V}{I} \quad (1)$$

The surface roughness of both the as-prepared and irradiated FLG/MLG samples were determined using the tapping mode of Atomic Force Microscopy (AFM) (AFM5500M system by Hitachi).

Elemental analysis of the as-prepared and irradiated MLG samples was done using an energy dispersive x-ray spectroscopy (EDX) detector (Model: XFlash 6|100, Bruker Scientific LLC), which was attached to the field-emission scanning electron microscope (FESEM). The electron accelerating voltage was 15 kV while the working distances for imaging and EDS were 8 and 15 mm, respectively.

Results and Discussions

Figure 2(a) and 2(b) depicts the FESEM images of the graphene nanoplatelet films for the FLG and MLG samples, respectively. The sample showed high-density graphene nanoplatelets which were uniformly distributed over an area of up to 20 μm^2. These nanoplatelets were very thin and highly transparent, with an average size between 100-150 nm, clearly implying the formation of FLG nanoplatelets. Thicker graphene flakes were observed for the MLG sample, which was shown from the contrast of the electron images, compared to the FLG sample, which indicated an elevation of the graphene layers in the sample (Kochat et al. 2011).

The respective Raman spectra of the FLG and MLG samples are depicted in Figure 2(c) and 2(d). The Raman spectra displayed the typical graphene-based Raman vibrational bands with its Raman shift positions at D (~1350 cm^{-1}), G (~1591 cm^{-1}), D' (~1620 cm^{-1}), and 2D (~2698 cm^{-1}). The G band is typically attributed to the in-plane vibrations of the sp^2 bonded carbon atoms. In contrast, the D band is attributed to the out-of-plane vibration, which is due to the structural disorder/defects of graphene which are possibly induced by the impurities (Lee et al. 2016). It represents the disorder in the six-fold carbon ring which originates from the sp^2 microdomains of the bond angle disorder, which is in return induced by the sp^3 hybridisations (Dresselhaus et al. 2005). The 2D band is attributed to the bond stretching of the pairs of the sp^2 C=C bonds and the double resonance Raman scattering mode (Kumari et al. 2017; Zheng et al. 2015). In contrast to the D band, the D'-band occurred from the intra-valley double resonant process (Malard et al. 2009). The D' peak originated from the resonant phonons of the LA branch near Γ. This peak was activated from the crystal defect of graphene. The combination of the (D+D') mode appears at ~ 2941 cm^{-1} for all the films, which is directly associated with the defect's concentration.

The FLG sample showed an I_{2D}/I_G ratio of 0.83, and the FWHM 2D peak was approximately 91 cm^{-1} and possessed several graphene layer features (bilayers up to six layers), as reported by Karamat et al. (2015) and Wu et al. (2018). Generally, the peak intensity ratio of the 2D and G bands (I_{2D}/I_G) and peak's FWHM values are used to determine the number of layers of the graphene sheet, where I_{2D}/I_G >1 and the FWHM value of the 2D peak is around 30–40 cm^{-1} which indicates a single-layer of graphene sheet or flake (Anuar et al. 2021; Syed et al. 2015). Asif et al. (2015) showed that the formation of 3-4 layers of graphene grown on Copper foil substrate had an I_{2D}/I_G ratio of 0.79. The MLG sample had a smaller I_{2D}/I_G ratio (0.52) and broader FWHM value for the 2D peak (149.07 cm^{-1}), showing the multi-layer features of the graphene film. On the other hand, the number of layers in the MLG samples were expected to be lower than 20 as the D' band did not appear at 1620 cm^{-1}, which is typically presented in the graphite structure.

Figure 3 shows a comparative analysis of the Raman spectra between the as-prepared and irradiated samples for (a) FLG and (b) MLG films. Clearly, there was a substantial reduction in the Raman peak intensities for both samples after the irradiation with high-energy electron beam. This showed that the high-energy electron beam with 1.2 GeV had directly induced a permanent carbon atom displacement in the graphene sheets under the electron beam bombardment effect. Similar carbon-related peak reductions were observed by Slobodian et al. (2018) with a much lower irradiation electron energy of 3 keV.

Table 2 tabulates the details of the C-related vibrational bands obtained using the peak deconvolution method. A blueshift in the G- and 2D bands for both samples were observed after electron beam irradiation. It is much more significant in the MLG samples with 9.75 and 12.06 cm^{-1}, than the FLG sample with 1.63 and 7.8 cm^{-1}, respectively. This blueshift presumably resulted from either the p-type doping (Zheng et al. 2015), or the compression strain due to the carbon atom displacement, creating point defects in the graphene samples (Iqbal et al. 2012; Murakami, Kadowaki & Fujita 2013). The doping of graphene could be due to the disruption of graphene lattice structure from carbon atom displacement when the incident beams interact with the graphene, and formed covalent bond with doping molecules such as gas substance in the atmosphere (Liu, Teweldebrhan & Balandin 2011; Ryu et al. 2010). The doping substance

such as oxygen, water vapour and nitrogen cause changes in the electrical properties of graphene by n-or-p-doped graphene samples. Incorporation of the doping substances can happen at the edges via intermediate vacancies, defect states, and dangling bonds, showing significant increments in their I_D/I_G values (FLG ~ 1.78 and MLG ~ 2.11 after the electron beam irradiation). The electron beam irradiation produces point defects originating from the dislocation of carbon atoms, resulting in the modification of the graphene structure's atomic network (Slobodian et al. 2018; Song et al. 2013). However, this did not affect the graphene nanoplatelet layers, as shown by the I_{2D}/I_G ratios after the irradiation (as tabulated in Table 2).

Figure 4 depicts the survey-scan XPS spectra of the as-prepared and irradiated samples (FLG and MLG films). The spectra mainly consist of O 1s, C 1s, W 4f, and Ag 3d bands centred at 284.5, 529.5, 33.5, and 368.3 - 374 eV, respectively. The presence of impurities such as Ag (Figure 4(a) & 4(b)) and W peaks are attributed to the silver conducting paint and the metallic W catalyst nanoparticles, respectively. The narrow scan of XPS spectra of C bands centred at 284.5 eV, and their fitted components are shown in Figure 5. Typically, the C peak can be decomposed into four major constituents namely C=C, C-C=C, C-OH, and C-O-C bonds at 284.3, 284.6, 285.4, and 286.6 eV, respectively (Díaz et al. 1996; Lesiak et al. 2018). The C=C and C-C=C bands represented the sp^2 and sp^3 hybridised bonded C atoms with a 0.3 eV binding energy separation, which was

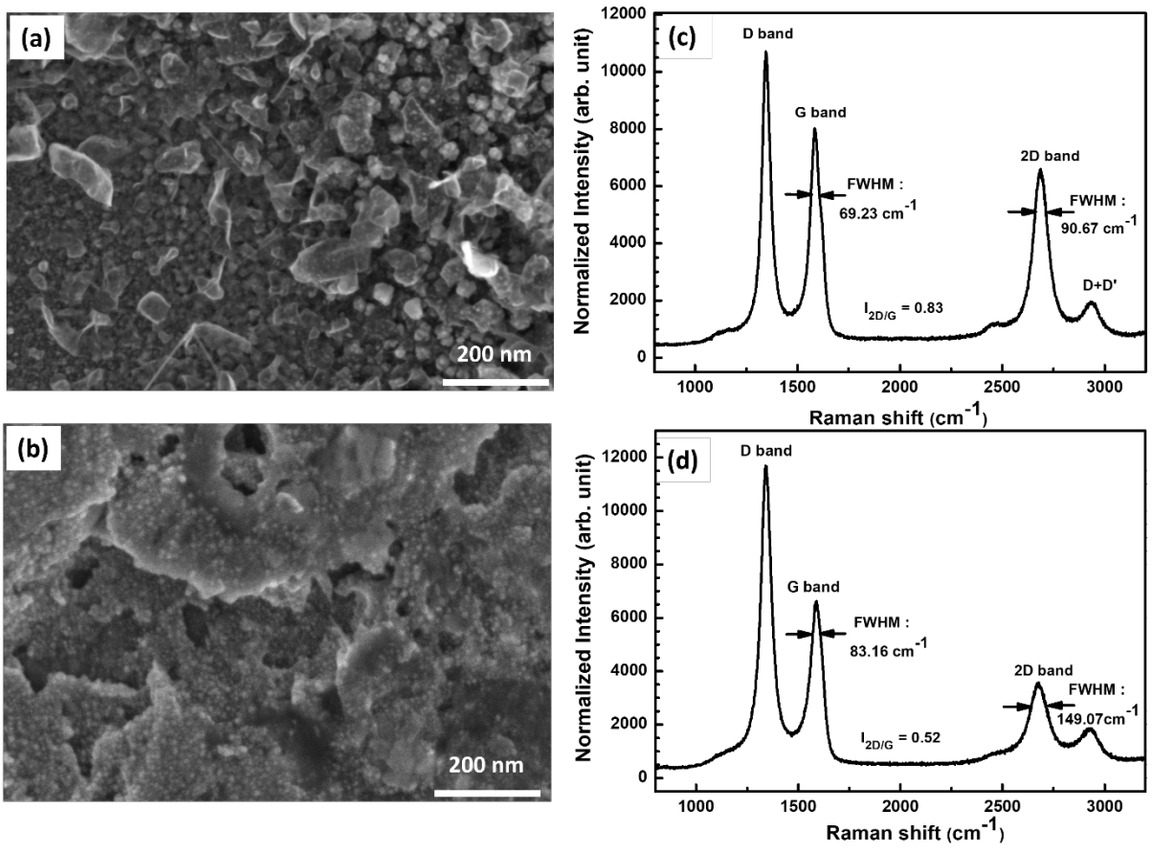

FIGURE 2. (a & b) FESEM images of the FLG and MLG samples. The scale bars of the images are indicated at the bottom of each figure. (c & d) Raman spectra of the FLG and MLG samples. The calculated I_{2D}/I_G ratio and FWHM values of the G and 2D bands are indicated in the figure

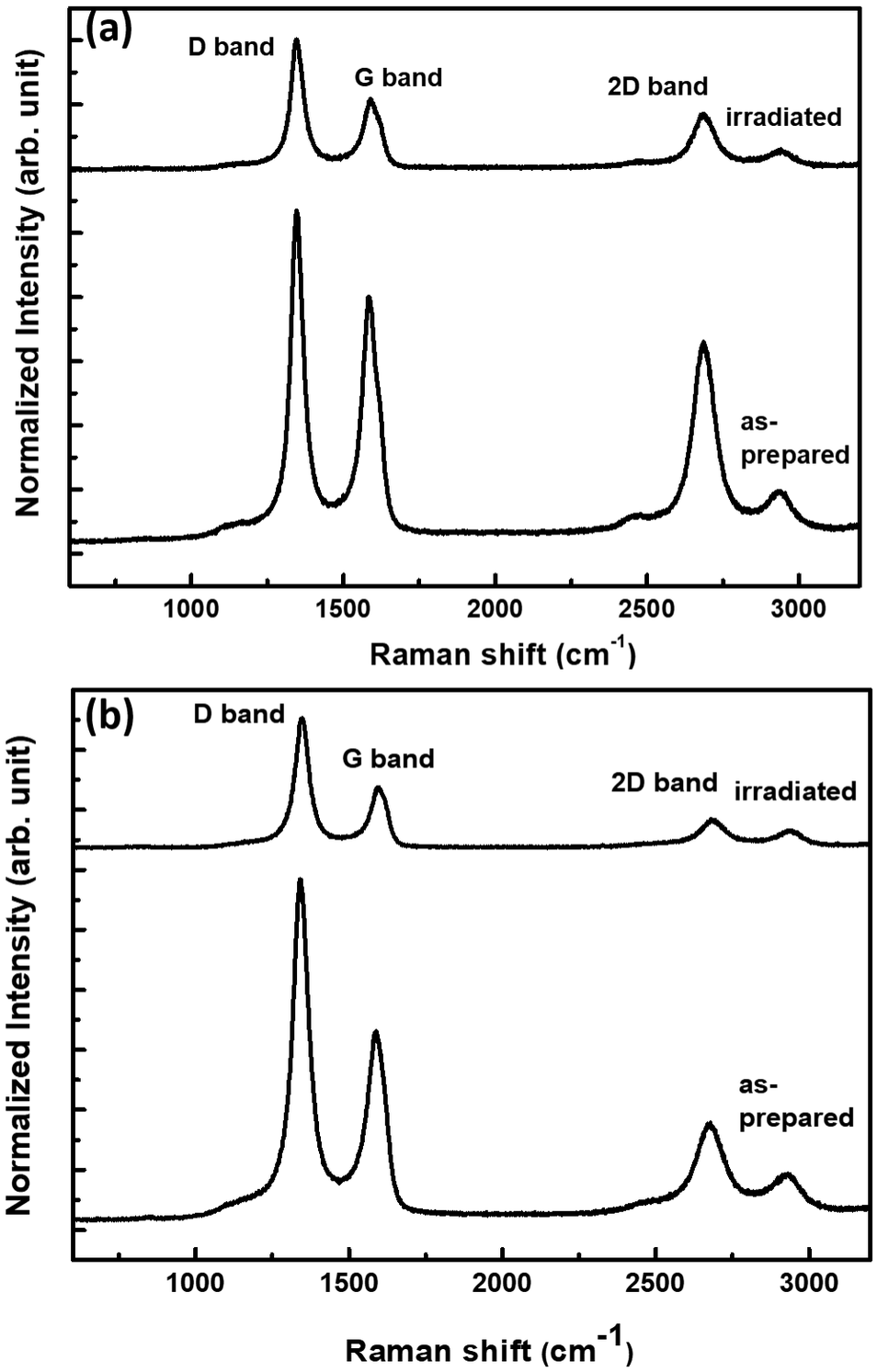

FIGURE 3. Raman spectra of as-prepared and irradiated graphene films (**a** FLG and **b** MLG)

TABLE 2. The values from the Raman spectrum of as-prepared and irradiated FLG and MLG

Sample		D band			G band			2D band			I_D/I_G	I_{2D}/I_G
Peak position (cm^{-1})		FWHM (cm^{-1})	I_D (counts)	Peak position (cm^{-1})	FWHM (cm^{-1})	I_G (counts)	Peak position (cm^{-1})	FWHM (cm-^{1})	I_{2D} (counts)			
FLG	as-prepared	1, 345.48	57.81	10, 714.56	1, 583.58	69.23	8, 015.84	2, 685.20	90.67	6, 620.32	1.34	0.83
	irradiated	1, 347.80	60.75	4, 255.40	1, 590.74	74.66	2, 395.64	2, 686.83	104.98	1, 925.23	1.78	0.80
MLG	as-prepared	1, 343.60	77.13	11, 703.60	1, 590.21	83.16	6, 886.99	2, 674.27	149.07	3, 562.14	1.70	0.52
	irradiated	1, 346.71	66.64	4, 449.33	1, 596.30	69.90	2, 112.64	2, 686.50	127.84	1, 037.66	2.11	0.49

associated with the threefold and fourfold-coordinated carbon atoms (Díaz et al. 1996). The sp^2/sp^3 hybridisation ratio was associated with the atomic density of the carbon structure, and represented the quality of the graphene in terms of its homogeneity and electronic properties (Haerle et al. 2002; Syed 2017; Yang et al. 2014). The sp^3 tetrahedral hybridisation bond of carbon atoms in the as-prepared samples was contributed by either edge defects of the individual graphene layers, or the intrinsic sp^3 defects in the FLG samples (Al-Harthi et al. 2012; Turgeon & Paynter 2001). The C-OH and C-O-C generally corresponded to the oxide hydroxyl groups and adventitious carbon contamination, respectively. The C-O-C bands are believed to have originated mainly from the edge defects of the nanoplatelets or flakes (Meyer et al. 2012).

The composition (in %) of each C-related component can be determined by dividing the integrated intensity of the component with the integrated intensity of the main peak. The percentage of C-related bands are tabulated in Table 3. The sp^2 C=C content reduced for both the FLG and MLG after the electron beam irradiation, which was approximately 8.5% and 2.7%, respectively. The carbon atoms dislocated from its graphene structure when it received higher electron beam energy than the displacement threshold energy of the sp^2 bonded carbon, in the range between 15-20 eV (Krasheninnikov & Banhart 2007). The high electron beams causes various electron-nuclei interactions, such as localised amorphisation or rehybridisation of the carbon atoms, which requires a minimum energy of 100 keV or above, as previously reported for multiwalled carbon nanotubes (Kumari et al. 2017). The electron-nuclei ionisation results in carbon atom displacements in the graphene structure. It also leads to multiple defects due to electron excitations (Meyer et al. 2012). The defects, such as oxidation and transformation of the sp^2 to sp^3 via hybridisation are shown by the changed C-O-C contents in the FLG and MLG, at a value of 14.6 and 2.03 %, respectively. Obviously, the hydroxyl groups (C-OH) have a much more negligible effect under the electron beam irradiation for the FLG and MLG. The obtained sp^2/sp^3 ratios of the as-prepared and irradiated FLG samples were 5.5 and 6.5, respectively, indicating an improved graphene structure quality after the irradiation (Al-Harthi et al. 2012). This was accompanied by an increment in the C-O-C content, which implied that the FLG was more sensitive to the electron beam irradiation due to its two-dimensional sheet characteristic, and the large surface area of the nanoplatelet structure. The effect of the beam irradiation was more significant in the FLG than MLG, due to the different thicknesses of the target with the high kinetic energy from the electron beam.

Figure 6 depicts the I-V curves of the as-prepared and irradiated FLG and MLG samples. The I-V curves of c-Si substrate and W nanoparticles deposited on the c-Si substrate are provided in the figure for control purposes. Obviously, the as-prepared FLG and MLG samples show an ohmic characteristic in the logarithmic scale with the measuring electrodes, implying that the metallic behaviour of graphene's unique electrical characteristic (Cooper et al. 2012), is naturally compatible, and shows low contact resistance towards Cr, Ti, Ni, and Pd (Xia et al. 2011). A relatively low turn-on voltage for the as-prepared MLG compared to the as-prepared FLG indicates that the MLG possesses lower resistivity compared to the FLG. The calculated sheet resistances of the as-prepared MLG and FLG films were 79.97 and 194.24 Ω/sq. The higher sheet resistance observed in the FLG compared to MLG might be due to the ambipolar characteristics of the thin films that resulted in heterogeneous current flow as a function of voltage (Bae et al. 2010). In addition, more significant lattice defects at the edges of graphene nanoplatelets which were grown using the HWCVD method contributed to the increase in the sheet resistance of the FLG (Cummings et al. 2014). It is observed that the I-V curves of c-Si n-type substrate and samples with W nanoparticles followed a non-linear Schottky junction characteristic, which was expected from the metal probe/semiconductor junction. The probe contact resistance may contribute to this case since the barrier height between the metal and semiconductor is very high, which is approximately 1-1.5 eV (Chandra et al. 2011). The linear curves observed for the as-prepared FLG and MLG samples suggest that the synthesised graphene films may reduce the contact resistance and barrier height between the probe and the samples. For the high-energy electron beam irradiated samples, it is found that the I-V curves consisted of two different conduction mechanism regions of ohmic and space charge-limited currents (SCLC). An ohmic conduction mechanism is dominant at low current supplies, where the logarithmic scale slope is almost equal to 1, following ohm's law for current conduction. At higher current supplies, the slope is measured at almost 2, indicating that the SCLC conduction mechanism obeyed the Mott-Gurney law of current conduction (Röhr

et al. 2018). This regime occurs when the injected charge concentration is higher than equilibrium charge concentration and establishes a space charge region adjacent to the injecting electrode (Elakrmi, Chaâbane & Ouada 2011). The W nanoparticles samples also showed high conductivity (48.5 mΩ/sq), owing to its metallic properties. This sheet resistance was comparable with the W thin films grown using the CVD technique, with a sheet resistance of 73.6 - 155 mΩ/sq, as reported in Li et al. (2012). The sheet resistance of the highly doped n-type c-Si substrate as calculated from the manufacturer's specification was also within a similar range (16 - 80 mΩ/sq).

The irradiated FLG and MLG samples showed similar electrical properties, as observed in the W nanoparticle samples with two types of conduction mechanism regions. However, for irradiated samples, the SCLC region had a higher slope value with n = 4.5 and 6, indicating that the region was regulated by the traps of the conduction region. The presence of the traps introduced by irradiation reduces the current at higher voltage supplies, originating from immobilised injected carriers in the traps (Vu 1970). Both irradiated FLG and MLG samples showed a similar sheet resistance, as calculated in the W nanoparticles sample, at 45 and 44 mΩ/sq, respectively. The changes in this conduction mechanism are probably due to the dislocation of the carbon atoms from the sample's surface, showing the W nanoparticles beneath the graphene layers. The non-ionising energy loss (NIEL) from the electron-nucleus atom scattering which exceeded the energy

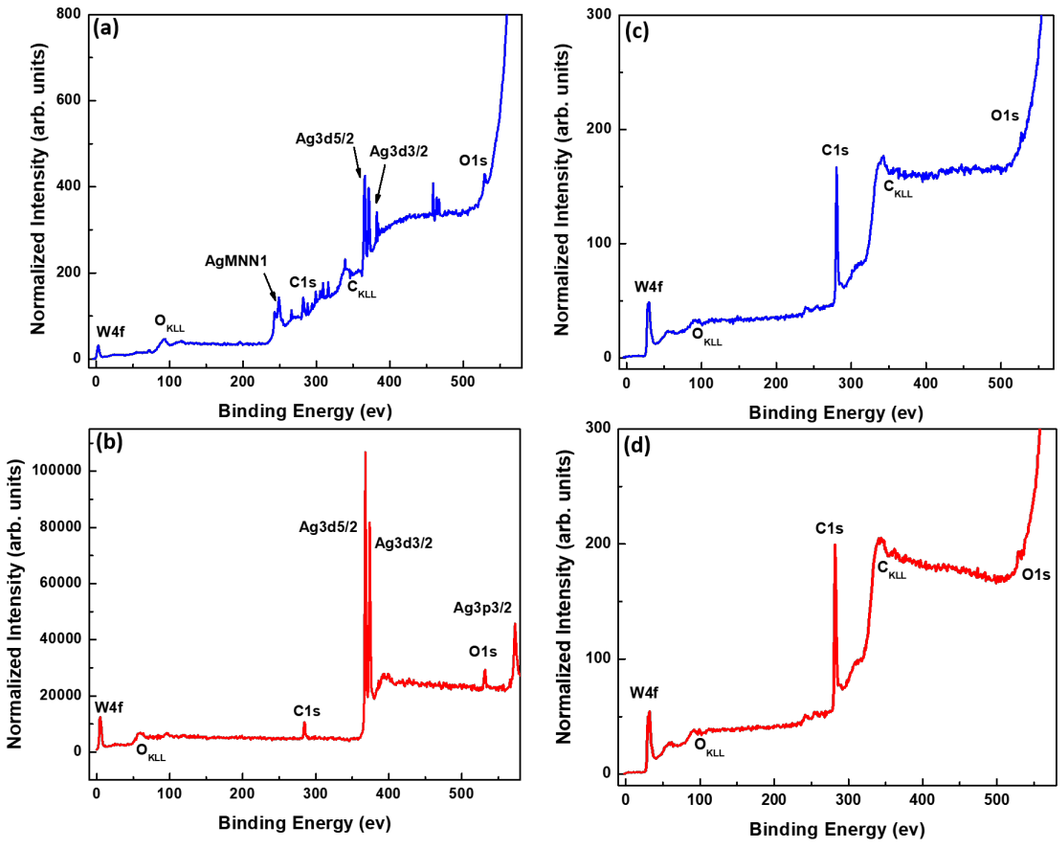

FIGURE 4. Survey-scan XPS spectra of (a & b) the as-prepared and irradiated samples of FLG, and (c & d) the as-prepared and irradiated samples of MLG, respectively

displacement threshold (E_d > 20 eV) in the graphitic structure was speculated to have contribute to this displacement effect in the graphene (Krasheninnikov & Banhart 2007; Liao et al. 2019). This is in agreement with the findings from the Monte Carlo simulation for the displacement damage in the graphene, as reported by Chatzikyriakou, Smyrnis and Chatwin (2014) and Liao et al. (2019) for high-energy interactions. These displacement effects have been reported to be much more dominant in FLG, due to the large cross-sections involved during interaction, compared to the MLG. The higher number of the graphene layers in the MLG reduces the scattering angle during the interaction and produces cascade collisions with lower defect creation. The changes in the I-V properties following the interaction with high-energy charged particle beams (proton) have previously been demonstrated (Kim et al. 2008; Slobodian et al. 2018).

The AFM topographic images provide information about the structural defects created from the interaction between high-energy electrons with the surface of the FLG and MLG. Figure 7(a) & 7(c) depicts the topographic images of the as-prepared FLG and MLG samples. The grainy topography of the as-prepared samples illustrates the graphene platelet structures with small spikes, originating from the tungsten nanoparticles on top of the graphene. The legend profiles indicate the maximum height of the samples, which agrees with the FLG ad MLG samples. The arithmetical mean roughness (Sa) of the as-prepared FLG sample (Sa = 10.90 nm) was

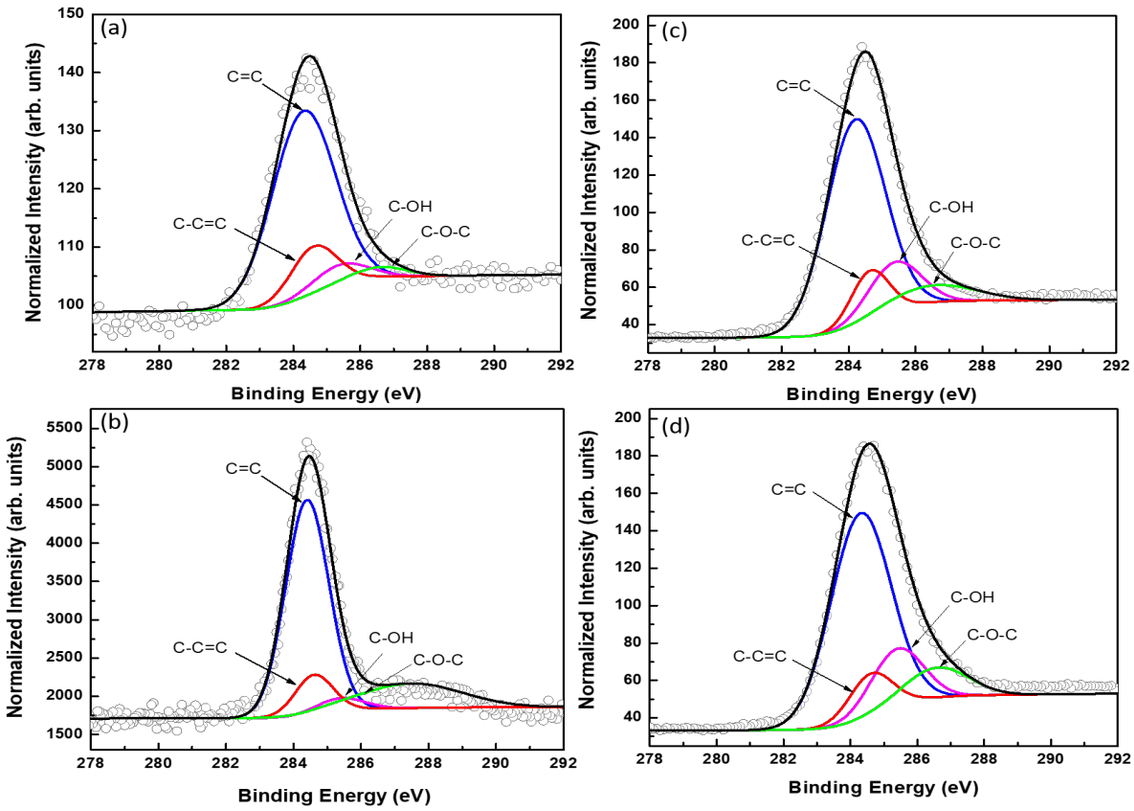

FIGURE 5. High-resolution scan XPS spectra of C 1s bands for (a & b) the as-prepared and irradiated samples of FLG, and (c & d) the as-prepared and irradiated samples of MLG, respectively

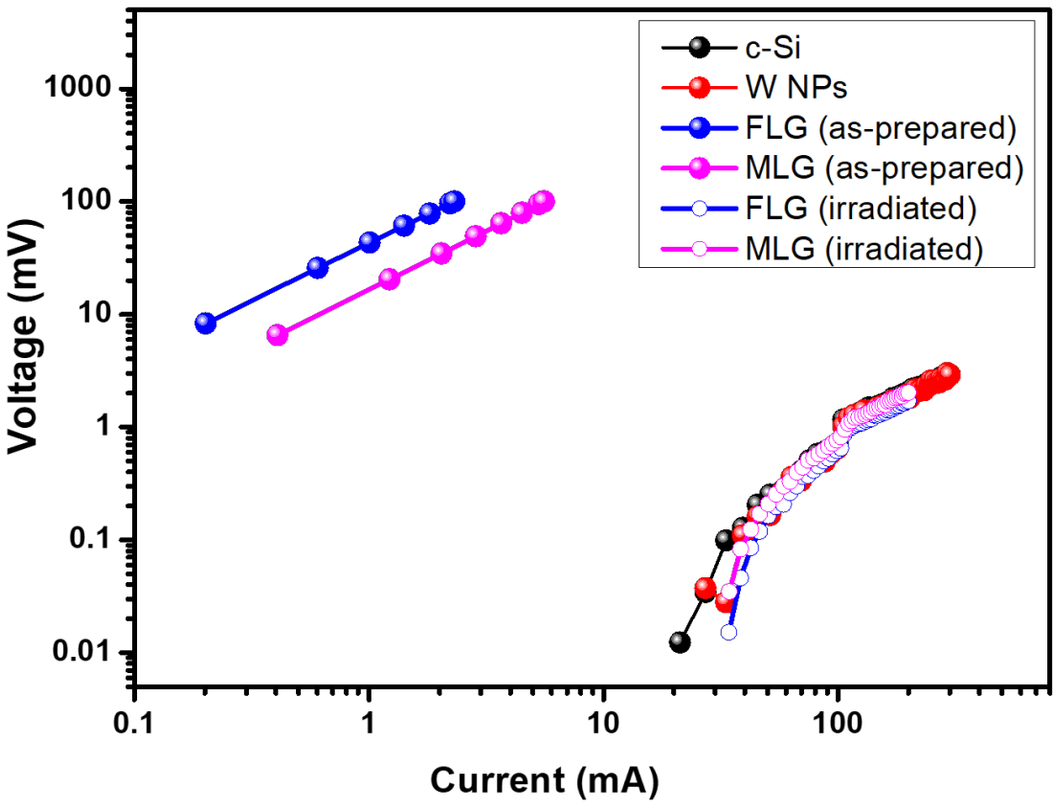

FIGURE 6. I-V curves as-prepared and irradiated samples of FLG and MLG. The I-V curves of c-Si substrate and W nanoparticles deposited on c-Si substrates as controls are provided in the figure

relatively lower than the MLG (Sa = 13.89 nm). This is similar to the root-mean-square (RMS) roughness (Sq) for both samples. Figure 7(b) and 7(d) shows the 2D and 3D topological profiles of the irradiated FLG and MLG, respectively. Interestingly, both samples (FLG & MLG) showed a slight reduction in the surface topography for the Sa and Sq values. The reductions were less than 3 nm, suggesting that the graphene samples possessed excellent stability against the high-energy electron beam irradiation, with an almost constant surface roughness and platelet grain size.

Despite the dislocation of carbon atoms in sp^2 and sp^3 bonds and the introduction of the surface and edge defects to the graphene structure, the surface topography of the graphene nanoplatelets remained, as shown clearly in Figure 7(b) and 7(d). The defects on the surface of FLG created by the high-energy electron beam were mainly vacancies and interstitials. The variation in the surface roughness on the FLG was most likely attributed to the surface and edge defects involving the low threshold displacement energy from the electron beams. The findings obtained herein are in line with the previous work showing that high-energy electron beams induced more surface defects on monolayer-graphene than those with a few-layers of graphene (Mathew et al. 2011). The more negligible effect created by the electron beam irradiation on the MLG sample was possibly due to its multi-layer structure and stability against the electron beam irradiation.

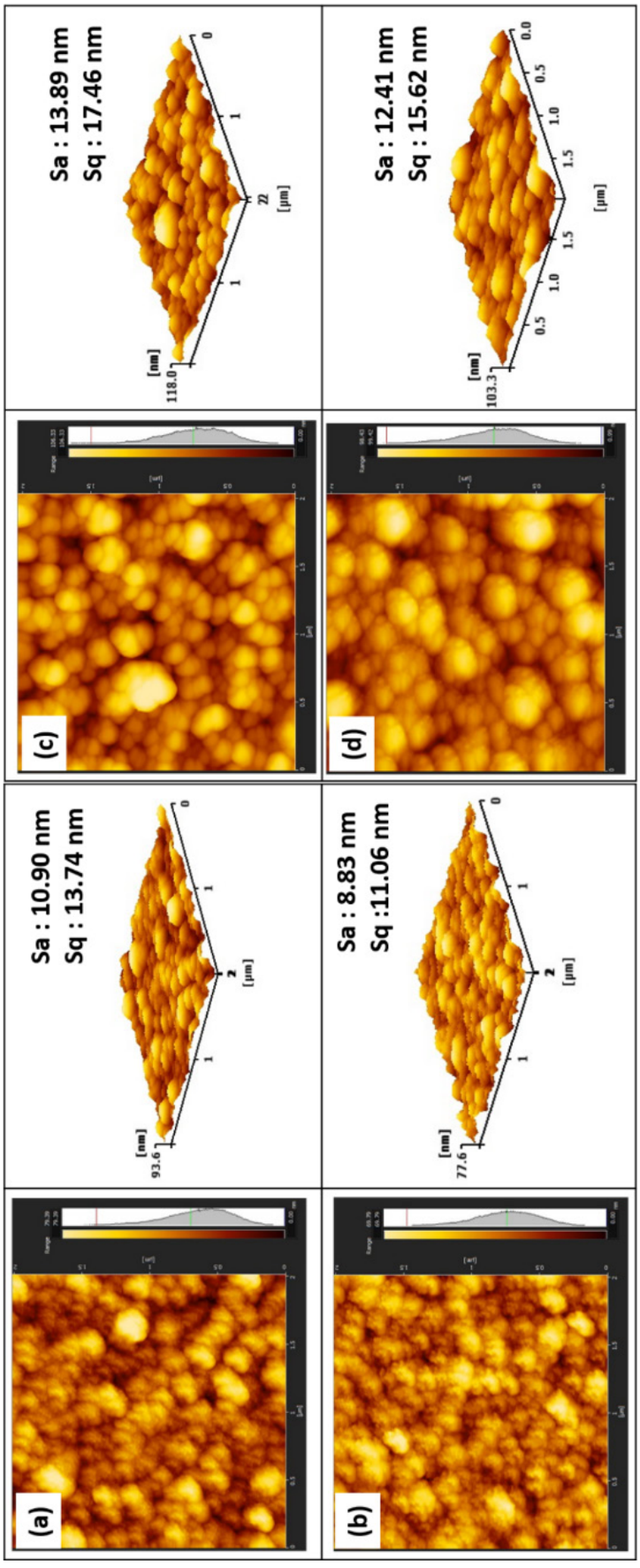

FIGURE 7. 2D and 3D AFM images of (a & b) the as-prepared and irradiated samples of FLG, and (c & d) as-prepared and irradiated samples of MLG, respectively

TABLE 3. Chemical composition of as-prepared and irradiated FLG and MLG samples analysed from XPS spectra

Sample		Chemical composition (%)			
		C=C (284.3 eV)	C-C=C (286.6 eV)	C-OH (285.4 eV)	C-O-C (286.6 eV)
FLG	as-prepared	76.17	13.85	6.58	3.40
	irradiated	67.63	10.47	3.86	18.04
MLG	as-prepared	68.17	10.13	13.76	7.94
	irradiated	65.40	9.34	15.29	9.97

CONCLUSIONS

The structure, chemical composition, and surface morphology of the FLG and MLG nanoplatelets films irradiated with high-energy electron beam were demonstrated herein. The results demonstrated that the 1.2 GeV high-energy electron beam irradiation with a dosage of 1.2×10^9 e^-/cm^2 greatly increased the surface and edge defects on the FLG. These defects were mainly attributed to the carbon atom displacements and oxidation due to the electron beams and graphene's surface interaction. The electron-induced doping was shown by the blue-shifted in the G- and 2D bands, of which, it was much more significant in the MLG. The findings of the study provided a preliminary insight into how the high-energy electron beam affects the 2D layered graphene.

ACKNOWLEDGMENTS

This work was supported by the the Ministry of Higher Education Fundamental Research Grant Scheme (FRGS/1/2020/STG07/UM/02/8). The authors extend their appreciation to the scientists at the Beam-Test Facility (BTF) and Photoemission Spectroscopy (PES) synchrotron beamlines 3.2(a) at the Synchrotron Light Research Institute, Thailand, for their technical assistance and beam-time support. Nurul Hidayah Mohamad Nor is also grateful to the Ministry of Higher Education (MOHE), and University Malaya (UM), for the scholarship support.

REFERENCES

Al-Harthi, S.H., Elzain, M., Al-Barwani, M., Kora'a, A., Hysen, T., Myint, M.T. & Anantharaman, M.R. 2012. Unusual surface and edge morphologies, sp^2 to sp^3 hybridized transformation and electronic damage after Ar^+ ion irradiation of few-layer graphene surfaces. *Nanoscale Research Letters* 7: 466. https://doi.org/10.1186/1556-276x-7-466

Ang, P.K., Chen, W., Wee, A.T. & Loh, K.P. 2008. Solution-gated epitaxial graphene as pH sensor. *Journal of the American Chemical Society* 130(44): 14392-14393. https://doi.org/10.1021/ja805090z

Anuar, N.A., Nor, N.H., Awang, R. binti, Nakajima, H., Tunmee, S., Tripathi, M., Dalton, A. & Goh, B.T. 2021. Low-temperature growth of graphene nanoplatelets by hot-wire chemical vapour deposition. *Surface and Coatings Technology* 411: 126995. https://doi.org/10.1016/j.surfcoat.2021.126995

Asif, M., Tan, Y., Pan, L., Li, J., Rashad, M. & Usman, M. 2015. Thickness controlled water vapors assisted growth of multilayer graphene by ambient pressure chemical vapor deposition. *The Journal of Physical Chemistry C* 119(6): 3079-3089. https://doi.org/10.1021/jp510106w

Bae, S., Kim, H., Lee, Y., Xu, X., Park, J-S., Zheng, Y., Balakrishnan, J., Lei, T., Ri Kim, H., Song, Y.I., Kim, Y-J., Kim, K.S., Özyilmaz, B., Ahn, J-H., Hong, B.H. & Iijima, S. 2010. Roll-to-roll production of 30-inch graphene films for transparent electrodes. *Nature Nanotechnology* 5(8): 574-578. https://doi.org/10.1038/nnano.2010.132

Chandra, N., Sharma, V., Chung, G.Y. & Schroder, D.K. 2011. Four-point probe characterization of 4H silicon carbide. *Solid-State Electronics* 64(1): 73-77. https://doi.org/10.1016/j.sse.2011.07.004

Chatzikyriakou, E., Smyrnis, C. & Chatwin, C. 2014. Monte Carlo simulation of electron and proton irradiation of carbon nanotube and graphene transistors. *Advances in Microelectronic Engineering (AIME)* 2(2): 33-37.

Childres, I., Jauregui, L.A., Foxe, M., Tian, J., Jalilian, R., Jovanovic, I. & Chen, Y.P. 2010. Effect of electron-beam irradiation on graphene field effect devices. *Applied Physics Letters* 97(17): 173109. https://doi.org/10.1063/1.3502610

Cooper, D.R., D'Anjou, B., Ghattamaneni, N., Harack, B., Hilke, M., Horth, A., Majlis, N., Massicotte, M., Vandsburger, L., Whiteway, E. & Yu, V. 2012. Experimental review of graphene. ISRN *Condensed Matter Physics* 2012: 501686. https://doi.org/10.5402/2012/501686

Cummings, A.W., Duong, D.L., Nguyen, V.L., Van Tuan, D., Kotakoski, J., Barrios Vargas, J.E., Lee, Y.H. & Roche, S. 2014. Charge transport in polycrystalline graphene: Challenges and opportunities. *Advanced Materials* 26(30): 5079-5094. https://doi.org/10.1002/adma.201401389

Díaz, J., Paolicelli, G., Ferrer, S. & Comin, F. 1996. Separation of the sp^3 and sp^2 components in the C1*s* photoemission spectra of amorphous carbon films. *Physical Review B* 54(11): 8064-8069. https://doi.org/10.1103/physrevb.54.8064

Dresselhaus, M.S., Dresselhaus, G., Saito, R. & Jorio, A. 2005. Raman spectroscopy of carbon nanotubes. *Physics Reports* 409(2): 47-99.

Elakrmi, E., Chaâbane, R.B. & Ouada, H.B. 2011. Structure and electrical properties of nanostructured zinc oxide films prepared for optoelectronic applications. *Physical Sciences* 2(1): ea0111. https://doi.org/https://akademeia.ca/pdf/vol2-iss1/Elakrmietal(2012)-2-1-ea0111.pdf

Greczynski, G. & Hultman, L. 2020. X-ray photoelectron spectroscopy: Towards reliable binding energy referencing. *Progress in Materials Science* 107: 100591. https://doi.org/10.1016/j.pmatsci.2019.100591

Haerle, R., Riedo, E., Pasquarello, A. & Baldereschi, A. 2002. sp^2/sp^3 hybridization ratio in amorphous carbon from C1*s* core-level shifts: X-ray photoelectron spectroscopy and first-principles calculation. *Physical Review B* 65: 045101.

Iqbal, M.Z., Kumar Singh, A., Iqbal, M.W., Seo, S. & Eom, J. 2012. Effect of e-beam irradiation on graphene layer grown by chemical vapor deposition. *Journal of Applied Physics* 111(8): 084307. https://doi.org/10.1063/1.4704197

Kang, J., Duan, Y., Gao, W., Li, H., Li, C., Zhao, X. & Zhu, C. 2022. Transparency of graphene membranes to eV-scale electrons. *Nuclear Instruments and Methods in Physics Research Section A: Accelerators, Spectrometers, Detectors and Associated Equipment* 1031:166521.

Karamat, S., Sonuşen, S., Dede, M., Uysallı, Y., Özgönül, E. & Oral, A. 2015. Coalescence of few layer graphene grains grown by chemical vapor deposition and their stacking sequence. *Journal of Materials Research* 31(1): 46-54. https://doi.org/10.1557/jmr.2015.350

Kim, K-J., Choi, J., Lee, H., Lee, H-K., Kang, T-H., Han, Y-H., Lee, B-C., Kim, S. & Kim, B. 2008. Effects of 1 MeV electron beam irradiation on multilayer graphene grown on 6H-sic(0001). *The Journal of Physical Chemistry C* 112(34): 13062-13064. https://doi.org/10.1021/jp805141e

Kittimanapun, K., Chanlek, N., Lakrathok, A. & Laoiamnongwong, N. 2018. Low intensity electron beam measurement at SLRI beam test facility. *Proc. 9th Int. Particle Accelerator Conf. (IPAC'18)*. pp. 4502-4504. https://doi.org/10.18429/JACoW-IPAC2018-THPMK086

Kittimanapun, K., Chanlek, N., Juntong, N., Cheedket, S., Klysubun, P., Krainara, S., Sittisard, K. & Supajeerapan, S. 2016. SLRI beam test facility development project. *Proc. 7th Int. Particle Accelerator Conf. (IPAC'16)*. pp. 2539-2541. doi: 10.18429/JACoW-IPAC2016-WEPMY002

Kochat, V., Nath Pal, A., Sneha, E.S., Sampathkumar, A., Gairola, A., Shivashankar, S.A., Raghavan, S. & Ghosh, A. 2011. High contrast imaging and thickness determination of graphene with in-column secondary electron microscopy. *Journal of Applied Physics* 110(1): 014315. https://doi.org/10.1063/1.3608062

Krasheninnikov, A.V. & Banhart, F. 2007. Engineering of nanostructured carbon materials with electron or ion beams. *Nature Materials* 6(10): 723-733. https://doi.org/10.1038/nmat1996

Kumari, R., Singh, F., Yadav, B.S., Kotnala, R.K., Peta, K.R., Tyagi, P.K., Kumar, S., Puri, N.K. 2017. Ion irradiation-induced, localized sp^2 to sp^3 hybridized carbon transformation in walls of multiwalled carbon nanotubes. *Nuclear Instruments and Methods in Physics Research Section B: Beam Interactions with Materials and Atoms*, 412 : 115–122. https://doi.org/10.1016/j.nimb.2017.09.019

Lee, C., Wei, X., Kysar, J.W. & Hone, J. 2008. Measurement of the elastic properties and intrinsic strength of monolayer graphene. *Science* 321(5887): 385-388. https://doi.org/10.1126/science.1157996

Lee, C., Kim, J., Kim, S., Chang, Y.J., Kim, K.S., Hong, B. & Choi, E.J. 2016. Strong hole-doping and robust resistance-decrease in proton- irradiated graphene. *Nature Publishing Group* 6: 21311.

Lesiak, B., Kövér, L., Tóth, J., Zemek, J., Jiricek, P., Kromka, A. & Rangam, N. 2018. C sp^2/sp^3 hybridisations in carbon nanomaterials - XPS and (X)AES study. *Applied Surface Science* 452: 223-231. https://doi.org/10.1016/j.apsusc.2018.04.269

Li, Y., Li, J., Jia, C. & Liu, X. 2012. Fabrication of tungsten films by metallorganic chemical vapor deposition. *International Journal of Minerals, Metallurgy, and Materials* 19(12): 1149-1153.

Liao, W., Alles, M.L., Zhang, E.X., Fleetwood, D.M., Reed, R.A., Weller, R.A. & Schrimpf, R.D. 2019. Monte Carlo simulation of displacement damage in graphene. *IEEE Transactions on Nuclear Science* 66(7): 1730-1737.

Lin, Y.M., Jenkins, K.A., Valdes-Garcia, A., Small, J.P., Farmer, D.B. & Avouris, P. 2009. Operation of graphene transistors at gigahertz frequencies. *Nano Letters* 9(1): 422-426. https://doi.org/10.1021/nl803316h

Liu, G., Teweldebrhan, D. & Balandin, A.A. 2011. Tuning of graphene properties via controlled exposure to electron beams. *IEEE Transactions on Nanotechnology* 10(4): 865-870. https://doi.org/10.1109/tnano.2010.2087391

Lu, G., Ocola, L.E. & Chen, J. 2009. Reduced graphene oxide for room-temperature gas sensors. *Nanotechnology* 20(44): 445502. https://doi.org/10.1088/0957-4484/20/44/445502

Malard, L.M., Pimenta, M.A., Dresselhaus, G. & Dresselhaus, M.S. 2009. Raman spectroscopy in graphene. *Physics Reports* 473(5-6): 51-87.

Mathew, S., Chan, T.K., Zhan, D., Gopinadhan, K., Barman, A.R., Breese, M.B.H., Dhar, S., Shen, Z.X., Venkatesan, T. & Thong, J.T.L. 2011. The effect of layer number and substrate on the stability of graphene under MeV proton beam irradiation. *Carbon* 49(5): 1720-1726. https://doi.org/10.1016/j.carbon.2010.12.057

Meyer, J.C., Eder, F., Kurasch, S., Skakalova, V., Kotakoski, J., Park, H.J., Roth, S., Chuvilin, A., Eyhusen, S., Benner, G., Krasheninnikov, A.V. & Kaiser, U. 2012. Accurate measurement of electron beam induced displacement cross sections for single-layer graphene. *Physical Review Letters* 108: 196102, Erratum 110: 239902. https://doi.org/10.1103/physrevlett.108.196102

Moser, J., Barreiro, A. & Bachtold, A. 2007. Current-induced cleaning of graphene. *Applied Physics Letters* 91(16): 163513. https://doi.org/10.1063/1.2789673

Murakami, K., Kadowaki, T. & Fujita, J. 2013. Damage and strain in single-layer graphene induced by very-low-energy electron-beam irradiation. *Applied Physics Letters* 102: 043111.

Nor, N.H.M., Anuar, N.A., Abdullah, W.A.T.W., Goh, B.T. & Yahya, M.F.Z.R. 2022. A Geant4 simulation on the application of multi-layer graphene as a detector material in high-energy physics. *Sains Malaysiana* 51(10): 3423-3436.

Robinson, J.T., Perkins, F.K., Snow, E.S., Wei, Z. & Sheehan, P.E. 2008. Reduced graphene oxide molecular sensors. *Nano Letters* 8(10): 3137-3140. https://doi.org/10.1021/nl8013007

Röhr, J.A., Moia, D., Haque, S.A., Kirchartz, T. & Nelson, J. 2018. Exploring the validity and limitations of the mott–gurney law for charge-carrier mobility determination of semiconducting thin-films. *Journal of Physics: Condensed Matter* 30(10): 105901. https://doi.org/10.1088/1361-648x/aaabad

Ryu, S., Liu, L., Berciaud, S., Yu, Y., Liu, H., Kim, P., Flynn, G.W. & Brus, L.E. 2010. Atmospheric oxygen binding and hole doping in deformed graphene on a SiO_2 substrate. *Nano Lett.* 10(12): 4944-4951.

Schedin, F., Geim, A.K., Morozov, S.V., Hill, E.W., Blake, P., Katsnelson, M.I. & Novoselov, K.S. 2007. Detection of individual gas molecules adsorbed on graphene. *Nature Materials* 6(9): 652-655. https://doi.org/10.1038/nmat1967

Serry, M., Sharaf, A.H., Emira, A., Abdul-Wahed, A. & Gamal, A. 2015. Nanostructured graphene–Schottky junction low-bias radiation sensors. *Sensors and Actuators A: Physical* 232: 329-340. https://doi.org/10.1016/j.sna.2015.04.031

Shulman, H. & Ginell, W.S. 1970. *Nuclear and Space Radiation Effects on Materials*. NASA Space Vehicle Design Criteria (Structures).

Slobodian, O.M., Tiagulskyi, S.I., Nikolenko, A.S., Stubrov, Y., Gomeniuk, Y.V., Lytvyn, P.M. & Nazarov, A.N. 2018. Micro-raman spectroscopy and electrical conductivity of graphene layer on SIO_2 dielectric subjected to electron beam irradiation. *Materials Research Express* 5(11): 116405. https://doi.org/10.1088/2053-1591/aadde3

Song, W., Lee, S. Il, Kim, Y., Jung, D.S., Jung, M.W., An, K.S. & Park, C.Y. 2013. Effect of MeV electron beam irradiation on graphene grown by thermal chemical vapor deposition. *Japanese Journal of Applied Physics* 52(12).

Syed, M.H. 2017. Growth and characterization of graphene and graphene/Copper oxide nanocomposites by hot-filament thermal chemical vapor deposition for flexible pressure sensor application. University of Malaya. Thesis (Unpublished) http://studentsrepo.um.edu.my/7208/

Syed, M.H., Chong, S.K., Huang, N.M. & Abdul Rahman, S. 2015. Fabrication of high-quality graphene by hot-filament thermal chemical vapor deposition. *Carbon* 86: 1-11.

Teweldebrhan, D. & Balandin, A.A. 2009. Modification of graphene properties due to electron-beam irradiation. *Applied Physics Letters* 94(1): 013101. https://doi.org/10.1063/1.3062851

Turgeon, S. & Paynter, R.W.U. 2001. On the determination of carbon sp^2/sp^3 ratios in polystyrene-polyethylene copolymers by photoelectron spectroscopy. *Thin Solid Films* 394(1): 44-48.

Vu, Q.T. 1970. *Space-charge-limited current in fast neutron irradiated silicon.* Dissertation (Ph.D.), California Institute of Technology. https://doi.org/10.7907/T93C-DG21

Warbinek, J., Leimbach, D., Lu, D., Wendt, K., Pegg, D. J., Yurgens, A. & Welander, J. 2019. A graphene-based neutral particle detector. *Applied Physics Letters* 114(6): 61902.

Wu, J-B., Lin, M-L., Cong, X., Liu, H-N. & Tan, P.H. 2018. Raman spectroscopy of graphene-based materials and its applications in related devices. *Chemical Society Reviews* 47(5): 1822-1873. https://doi.org/10.1039/c6cs00915h

Xia, F., Perebeinos, V., Lin, Y-M., Wu, Y. & Avouris, P. 2011. The origins and limits of metal–graphene junction resistance. *Nature Nanotechnology* 6(3): 179-184. https://doi.org/10.1038/nnano.2011.6

Yang, X.H., Guo, W., Yang, S. & Hou, Y. 2014. A free radical assisted strategy for preparing ultra- small Pt decorated CNTs as a highly efficient counter electrode for dye-sensitized solar cells. *Journal of Material Chemistry A* 3: 614-619.

Zhang, T., Cheng, Z., Wang, Y., Li, Z., Wang, C., Li, Y. & Fang, Y. 2010. Self-assembled 1-octadecanethiol monolayers on graphene for mercury detection. *Nano Letters* 10(11): 4738-4741. https://doi.org/10.1021/nl1032556

Zheng, X., Chen, W., Wang, G., Yu, Y., Qin, S., Fang, J., Wang, F. & Zhang, X.A. 2015. The Raman redshift of graphene impacted by gold nanoparticles. *AIP Advances* 5(5): 057133. https://doi.org/10.1063/1.4921316

*Corresponding author; email: nurulhidayah@um.edu.my